Climatology of Gravity Wave Activity From Two Martian Years of ACS/TGO Observations

Ekaterina D. Starichenko[1], Alexander S. Medvedev[2], Denis A. Belyaev[1], Erdal Yiğit[3], Anna A. Fedorova[1], Oleg I. Korablev[1], Alexander Trokhimovskiy[1], Franck Montmessin[4], Paul Hartogh[2]

[1]Space Research Institute of the Russian Academy of Sciences (IKI), Moscow, Russia
[2]Max Planck Institute for Solar System Research, Göttingen, Germany
[3]Department of Physics and Astronomy, George Mason University, Fairfax, VA, USA
[4]LATMOS/IPSL, Guyancourt, France

Key Points:

- GWs' parameters for two Martian years from temperature profiles of ACS spectrometers have been obtained
- The seasonally varying distributions of the GWs' drag agree well with predictions of general circulation models
- Observations reveal high-latitude enhancement of GW activity in both hemispheres during the global dust storm

Corresponding author: Ekaterina Starichenko, `starichenko.ed@phystech.edu`

Abstract

We report the gravity wave (GW) statistics accumulated over two Martian years from the second half of Martian Year 34 (MY34) to the middle of MY36 (May 2018 - February 2022). The observations were performed by the middle- and near-infrared (MIR and NIR, respectively) spectrometers of Atmospheric Chemistry Suite (ACS) on board ExoMars Trace Gas Orbiter (TGO). Temperature profiles obtained independently of both channels during simultaneous measurements show a good agreement, thus providing verification and additional confidence in the data. GW parameters such as temperature fluctuations, potential energy per unit mass, and wave drag are retrieved at altitudes up to 160 km from the MIR channel and up to 100 km from the NIR channel. We present seasonal, intraday and latitude distributions of the wave potential energy and drag, serving to represent the wave activity and impact on the dynamics. A comparison of data obtained during the global dust storm (GDS) of MY34 with the corresponding period of MY35 without a storm reveals a reduction of GW activity in mid-latitudes in agreement with previous observations, and enhancement in the polar regions of both hemispheres, which was predicted by theoretical studies using simulations with a high-resolution circulation model. Seasonal variations of the derived GW activity can be linked to changes in the solar tide.

Plain Language Summary

Gravity waves with horizontal scales of tens and hundreds kilometers are present in atmospheres of all planets. They play an important role in the dynamics and thermodynamics of the middle and upper atmosphere of Mars through transporting the energy and momentum from the lower to the upper layers of atmosphere. The knowledge of their spatio-temporal variability is required for characterization of the atmospheric state and circulation. Two independent channels of the Atmospheric Chemistry Suite instrument on board the ExoMars Trace Gas Orbiter provided thousands of temperature profiles over two Martian years, which were used for retrieving wave characteristics. We present the climatology of gravity wave activity in the form of seasonal, latitudinal and local time distributions. They reveal a strong response of the gravity wave field to the global dust storm occurred in 2018. The derived distributions of the deceleration of the large-scale flow imposed by gravity waves can constrain global circulation models and improve their predictive capabilities.

1 Introduction

Gravity (or buoyancy) waves (GWs) originating from the balance of gravity and buoyancy forces are ubiquitous in all convectively stable atmospheres. They have been extensively studied in the terrestrial atmosphere, where their important role in the dynamics and vertical coupling of atmospheric layers has been recognized (e.g., see reviews by Fritts & Alexander, 2003; Yiğit & Medvedev, 2015). First GW-like signature in the atmosphere of Mars was detected in entry measurements of Viking 2 (Seiff & Kirk, 1976). Since then, GWs have been observed on Venus (R. E. Young et al., 1987), Jupiter (L. A. Young et al., 1997), Titan (Hinson & Tyler, 1983), Saturn (Brown et al., 2022) and other planets (see a recent review on GWs in planetary atmospheres by Medvedev & Yiğit, 2019). Recently, various GW-related phenomena in the Martian atmosphere and their impact on the whole atmosphere of Mars system have been reviewed (Yiğit, 2023).

In situ accelerometer measurements in the thermosphere of Mars performed during spacecraft aerobreaking demonstrated large amplitudes of GW-induced density disturbances and the associated wave drag (Keating et al., 1998; Creasey et al., 2006a; Fritts et al., 2006). The omnipresence of GWs in the lower Martian atmosphere and first characterization of the GW field were revealed using remote sensing techniques (Hinson et al., 1999; Creasey et al., 2006b; Wright, 2012; Nakagawa et al., 2020; Heavens et al., 2020).

They showed a varying spatio-temporal structure of the GW field and evidence for a limitation of amplitude growth with height, which is an indication of wave momentum transfer to the larger-scale flow (Ando et al., 2012).

GWs exist at all atmospheric heights. In situ measurements using the Neutral Gas and Ion Mass Spectrometer (NGIMS) on board the Mars Atmosphere and Evolution Mission (MAVEN) orbiter delivered a large body of GW statistics in the upper thermosphere (Yiğit et al., 2015; England et al., 2017; Terada et al., 2017; Leelavathi et al., 2020; Rao et al., 2021). In particular, the observations found an enhancement of GW activity during the global dust storm (GDS) that occurred in June 2018 (Martian year 34, MY34) (Leelavathi et al., 2020; Yiğit, Medvedev, Benna, & Jakosky, 2021). Conversely, observations with the Mars Climate Sounder instrument on board Mars Reconnaissance Orbiter have shown a reduction of such activity in the lower atmosphere (Heavens et al., 2020). Another existing controversy concerns the inverse relation between the amplitudes of GWs and the background temperature in the upper thermosphere. A number of studies attributed it to convective instability that limits wave amplitudes causing the so-called "saturation" (England et al., 2017; Terada et al., 2017; Vals et al., 2019), while Yiğit, Medvedev, and Hartogh (2021) argued that the inverse relation occurs because a colder background air reduces the scale height H, thus facilitating the exponential growth of amplitude, which is proportional to $1/2H$. Molecular diffusion and thermal conduction also exponentially grow with height in response to density decrease. They eventually exceed all other damping mechanisms in the thermosphere, and thereby significantly limits the wave growth.

GWs are generated in the lower atmosphere by a variety of mechanisms that vertically displace air parcels, e.g., flow over topography, convection, weather instabilities, etc. While propagating upward, they are partially filtered out by the background mean wind. Amplitudes of the surviving harmonics grow with height. Ultimately, the harmonics reach altitudes, where they are dissipated owing to a combination of nonlinear interactions, molecular diffusion, and thermal conduction, and deposit their momentum and energy to the ambient flow (Yiğit et al., 2008). This gravity wave-mean flow interaction produces acceleration/deceleration of the large-scale circulation, which is often called "GW drag". Its dynamical importance in the middle and upper atmosphere of Mars has been demonstrated with general circulation models (GCMs) where the effects of small-scale GWs are either parameterized (Medvedev et al., 2011a, 2011b; Gilli et al., 2020; Yiğit et al., 2018; Roeten et al., 2022), or explicitly resolved (Kuroda et al., 2015, 2016, 2019). These modeling studies have to be validated with observations, and many employed parameters constrained. Therefore, an observational characterization of the GW field and its spatio-temporal variation at all heights is of great importance.

The MIR spectrometer of Atmospheric Chemistry Suite (ACS) experiment on board the Trace Gas Orbiter (TGO) (Korablev et al., 2018) allows filling this gap in the knowledge of atmospheric variability by measuring vertical profiles of density and temperature between 20 and 160–180 km in the Martian atmosphere. The algorithm of retrieving GW profiles and their characteristics along with the first results of its application have been presented in detail in the work by Starichenko et al. (2021). The database of observations has been significantly extended since then. In this work, we present the results on GW activity obtained over the second half of the Martian year 34, the whole MY35 and the first half of the MY36. In addition, we analyzed the profiles measured by another ACS channel - near-IR (NIR). Although they cover altitudes only up to $\sim$100 km, their number (several thousand) adds significantly to the overall statistics.

The structure of this paper is the following. In Section 2, observations and temperature retrieval procedures from ACS are outlined. The methods of deriving the GW characteristics are described in Section 3. Section 4 presents the data coverage. Latitude-altitude distributions for four Martian seasons are given in Section 5, the impact of the global dust storm on the GW activity is discussed in Section 6, and local time variations are shown in Section 7. Conclusions are presented in Section 8.

2 Observations and Temperature Retrievals

The Atmospheric Chemistry Suite (ACS) is a part of the Trace Gas Orbiter (TGO), which represents the ESA-Roscosmos ExoMars 2016 collaborative mission. The instrument consists of three infrared channels (Korablev et al., 2018): near-IR (NIR, 0.73-1.6 μm), middle-IR (MIR, 2.3-4.2 μm), and thermal-IR (TIRVIM, 1.7-17 μm). In this work, we use the data obtained from the MIR and NIR spectrometric channels operating in the solar occultation mode since April 2018. ACS-MIR is a cross-dispersion echelle spectrometer that allows for retrieving temperature and density vertical profiles in the strong 2.7 μm CO_2 absorption band covering the broad altitude range of 20–180 km (Belyaev et al., 2021, 2022). ACS-NIR, an echelle spectrometer combined with an acousto-optic tunable filter, measures the atmospheric structure in 1.43 μm and 1.57 μm CO_2 bands at altitudes from 10 to 100 km (Fedorova et al., 2020, 2023). Both ACS MIR and NIR channels possess a high resolving power exceeding ∼25000, the signal-to-noise ratio of more than 1000, and sound the atmosphere with the vertical resolution of ∼1 km. During simultaneous occultations, the lines of sight (LOS) of both instruments target identical tangent points. This provides a confidential cross-validation between the retrieved atmospheric profiles. The altitude of the tangent points is determined as the closest distance between thr instrument's LOS and the areoid surface of the planet. The atmospheric transmission spectrum at each tangential altitude is obtained as a ratio of the solar spectrum transmitted through the atmosphere to the reference one measured at an altitude where the absorption at the given CO_2 band is negligible, that is 200 km for the MIR case and 130 km for NIR.

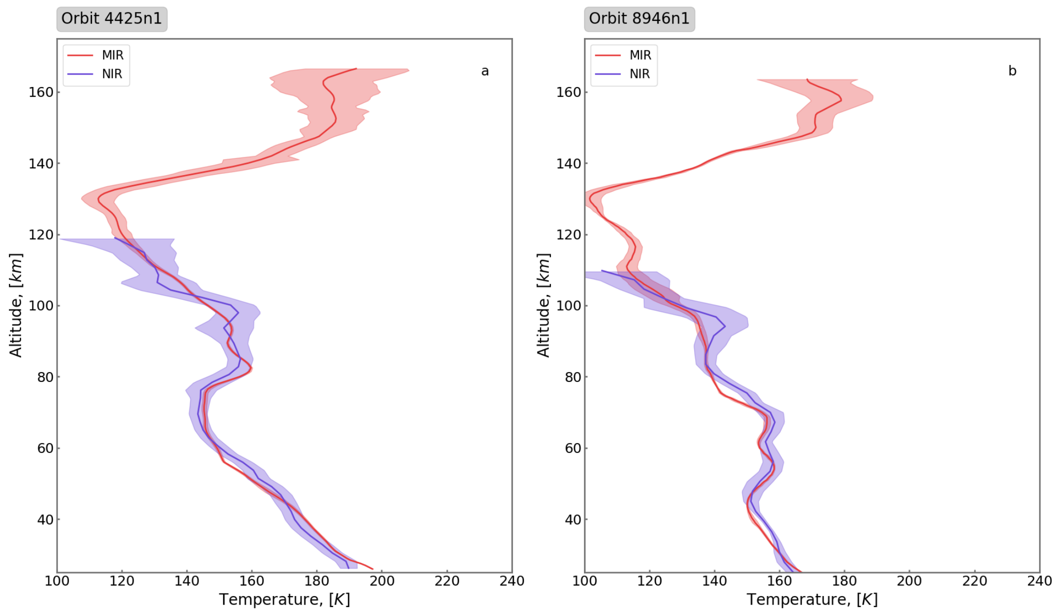

Figure 1. Vertical profiles of temperature derived from simultaneous ACS-MIR (red line) and ACS-NIR (blue line) occultations. Shaded area denotes the uncertainty of the measurements. Examples are from orbits a) 4425n1 (20 Nov 2018 MY34, L_s=291.7°, Lat=39.2°S) and b) 8946n1 (25 Nov 2019, MY35, L_s=111.7°, Lat=60.9°N).

The procedures of retrieving density and temperature vertical profiles from the transmission spectra of CO_2 are extensively described in the papers of Belyaev et al. (2021, 2022) for the MIR channel and of Fedorova et al. (2020, 2023) for the NIR channel. Profiles with estimated 1-σ errors exceeding 20 K have been removed from consideration based on expected wave amplitudes. Validation between simultaneously measured MIR and NIR profiles demonstrates a good coincidence below 100 km with dispersion of 5-10 K in more than 90% of occultations (Belyaev et al., 2022). When retrieving the GW parameters (see Section 3), the data were checked for reasonably smooth background temperature profiles (suitable for extracting waves) and for adequate values of the potential energy (<1000 J kg^{-1}). Anomalous values could be found either at inflection points of temperature profiles, such as around the mesopause, or near the top of the domain (80-100 km) for the NIR data. Such cases account for about 10-15% of all occultations, and they were excluded from our consideration.

In most of simultaneous observations, both the MIR and NIR individual profiles (Figures 1, 2a, 2d) along with the retrieved GW parameters (Figures 2b, 2c) closely match each other. Nevertheless, in some cases, the evaluated GW amplitudes and potential energy somewhat differ between two channels (see Figures 2d, 2e). The reason for that is in different altitude domains used for retrieving the NIR and MIR background temperature. Consequently, the maximum discrepancy occurs near the upper end (80-100 km) of the NIR profiles (Figures 2d, 2e). Overall, statistics of occultations at the MIR 2.7 μm CO_2 band are about 10 times less frequent than those at the NIR CO_2 spectra. Thus, in the analyses to be presented, we complement the MIR profiles with those from NIR, whenever measurements with MIR are not available.

3 Gravity Wave Characteristics

Separation of the observed temperature profile $T(z)$ into the background $\overline{T}$ and the GW-induced disturbance $T' = T - \overline{T}$ is an ambiguous procedure, because no unique partition exists. The wave component grossly depends on the definition of the mean temperature $\overline{T}$. The routine used in this work was described in detail and extensively tested in the paper by Starichenko et al. (2021). It was recently applied to retrievals of GWs in the thermosphere of Saturn (Brown et al., 2022). The mean vertical profile is determined by fitting cubic polynomials within sliding windows of 60 km width, effectively limiting the consideration to relatively short-scale GW harmonics with vertical wavelengths smaller than 30 km. The windows are shifted first from the bottom up and then downward with 7-km steps. Then, all the overlapping polynomials are averaged, and the final profile is smoothed over by a moving average procedure. The uppermost and lowest 4 km of each profile have to be dropped due to a spurious behavior of the fitted polynomials at the edges, which cannot otherwise be averaged. After the mean and wave components for each profile are derived, the Brunt-Väisälä frequency, wave amplitude, wave potential energy, vertical flux of horizontal momentum and GW drag can be determined. The Brunt-Väisälä frequency characterizes the convective stability of the atmosphere:

$$N^2 = \frac{g}{T}\left(\frac{dT}{dz} + \frac{g}{c_p}\right), \tag{1}$$

where g is the acceleration of gravity and c_p is the specific heat capacity at constant pressure. If N^2 approaches zero (or the temperature gradient approaches the dry adiabatic lapse rate), the stability decreases. When N^2 drops below zero, the atmosphere becomes convectively unstable and no longer supports GW propagation. Thus, GW harmonics experience strong dissipation and/or breaking in the regions of small or negative N^2.

Since GW harmonics usually propagate in wave packets, the observed instantaneous peaks and troughs do not fully characterize the wave amplitude. The latter (or "wave activity") is better represented by the envelope for temperature disturbances $|T'| = \sqrt{\overline{T'^2}}$. It is calculated by performing the Fourier decomposition in each 60-km sliding window

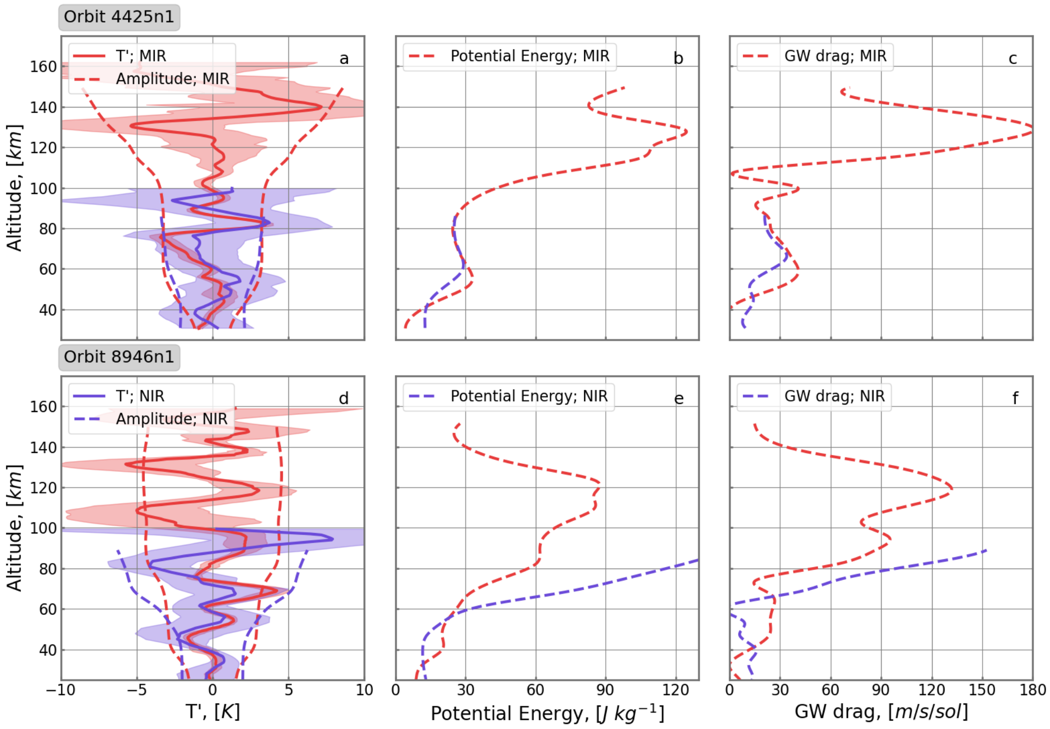

Figure 2. Wave characteristics retrieved for two representative measurements shown in Figure 1: orbits 4425n2 (upper row) and 8946n1 (lower row). The red and blue colors distinguish the MIR and NIR data correspondingly. In the left column (**a**, **d**), the solid lines represent wave-induced distributions of temperature T', dashed lines are for the wave packet envelopes $|T'|$, and shades indicate the errors. The middle column (**b**, **e**) compares the potential energy profiles, while the right column (**c**, **f**) presents the calculated GW drag.

and summation of contributions from all harmonics. The other useful measure of the wave field is the potential energy (per unit mass) E_p:

$$E_p = \frac{1}{2}\left(\frac{g}{N}\right)^2 \left(\frac{|T'|}{\overline{T}}\right)^2. \tag{2}$$

While $|T'|$ and E_p describe spatio-temporal distributions of the wave field itself, the vertical flux of horizontal momentum (per unit mass) quantifies the momentum transport by propagating harmonics. It is defined as $\mathbf{F} = (F_x, F_y, 0) = (\overline{u'w'}, \overline{v'w'}, 0)$, where u', v' and w' are the components of wave-induced disturbances of velocity in the zonal, meridional and vertical directions, correspondingly. The directional part of the flux cannot be inferred from a single vertical profile, however the absolute momentum flux $F = \sqrt{F_x^2 + F_y^2}$ (e.g., Ern et al., 2004, sect. 4) can be estimated:

$$F = \sum_{k_h, m} \frac{1}{2}\frac{k_h}{m}\left(\frac{g}{N}\right)^2 \left(\frac{|T'_{k,m}|}{\overline{T}}\right)^2. \tag{3}$$

The variables k_h and m in (3) are the horizontal and vertical wavenumbers, $|T'_{k,m}|$ is the amplitude of the corresponding harmonic, and the summation over all k_h and m is done. While amplitudes and vertical wavenumbers of particular harmonics are determined by the Fourier analysis, the horizontal wavenumber cannot be derived from a single vertical profile. Instead, it serves as a scaling factor, the value of which has to be assigned. In our analysis, the characteristic k_h^* was chosen considering that the densest atmospheric footprint at a target point in occultation experiments is ∼400-500 km horizontally, and harmonics with longer wavelengths remain unresolved. In our calculations, we assumed the horizontal wavelength $\lambda_h^* = 2\pi/k_h^* = 300$ km, which also agrees with that commonly used in GW parameterizations implemented into numerical GCMs (e.g., Yiğit et al., 2018). The momentum lost by a given breaking/dissipating harmonic is transferred to the background flow, thus producing its acceleration or deceleration, or imposing the so-called GW "drag"

$$a_h = \frac{1}{\bar{\rho}} \frac{d\bar{\rho}F}{dz}. \tag{4}$$

In (4), $\bar{\rho}$ denotes the mean density; the subscript h indicates that the acceleration occurs in the horizontal direction. Since the precise direction of F is not known, only absolute values of a_h can be determined from the observations. In the lower parts of the profiles, the amplitudes and the momentum flux F are small. This can lead to big differences of small values in the calculations of a_h, which can result in negative values. In order to avoid this non-physical behavior, we applied to F the iterative procedure described in the paper of Brown et al. (2022, Supporting Information S1).

Results of the derived wave characteristics described above are presented in Figure 2 for two representative occultations from Figure 1. For the first example (orbit 4425n1), not only the temperature profiles from MIR and NIR coincide, but the retrieved wave amplitudes and phases as well (Figure 2a). As a result, the envelopes of the wave packet determined from the MIR and NIR data agree well up to ∼90 km (Fig. 2b, 2c). However, for the second profile (orbit 8946n1), the amplitude and estimated potential energy disagree between MIR and NIR above 50 km (Fig. 2d, 2e), although short vertical-scale features in the temperature profile are resolved well. The altitude distribution of the wave drag agrees well up to ∼80 km for both orbits, peaking with 60 m s^{-1} sol^{-1} around 80 km (Figures 2c,f). Above this height, the temperature uncertainties significantly increase for the NIR data.

4 Description of the Data Coverage

The analyzed NIR and MIR measurements were taken over two Martian years (MY), between the second half of MY34 and the first half of MY36 (May 2018 - February 2022). For that period, the MIR 2.7 μm CO_2 band statistics encompasses ∼350 occultations in each hemisphere, while the NIR observations are performed ∼10 times more frequently. The seasonal-latitudinal coverage of individual orbits is presented in Figure 3 (upper row) as a function of the solar longitude L_s for the northern (left column) and southern (right column) hemispheres separately. Due to the solar occultation mode, the observations were performed either during sunrises or sunsets over morning or evening twilight. However, since the local time (LT) of the solar terminator varies with orbit and latitude, it may reach midday or midnight closer to the polar regions (Figures 3a,b).

To analyse the seasonal variability of the GW parameters, we grouped the individual vertical profiles into bins of 3° of L_s and 1 km of altitude. Thus, each bin represents an average of one to seven measured values. Since errors grow with height and profiles extend to different altitudes, the contribution of individual profiles in their top 20 km was weighted by the coefficient ranging from one to zero. The distributions for the GW drag and wave potential energy are plotted in the middle and lower panels of Figure 3, correspondingly. The upper altitude spread depends on season and latitude varying from 10-20 km to 140-150 km at aphelion and from 20-30 km to 160-170 km at perihelion, as clearly seen in the southern hemisphere (Figures 3d,f). An increased wave activity of up to 300-400 J kg^{-1} is observed in the winter hemispheres at the mesospheric and ther-

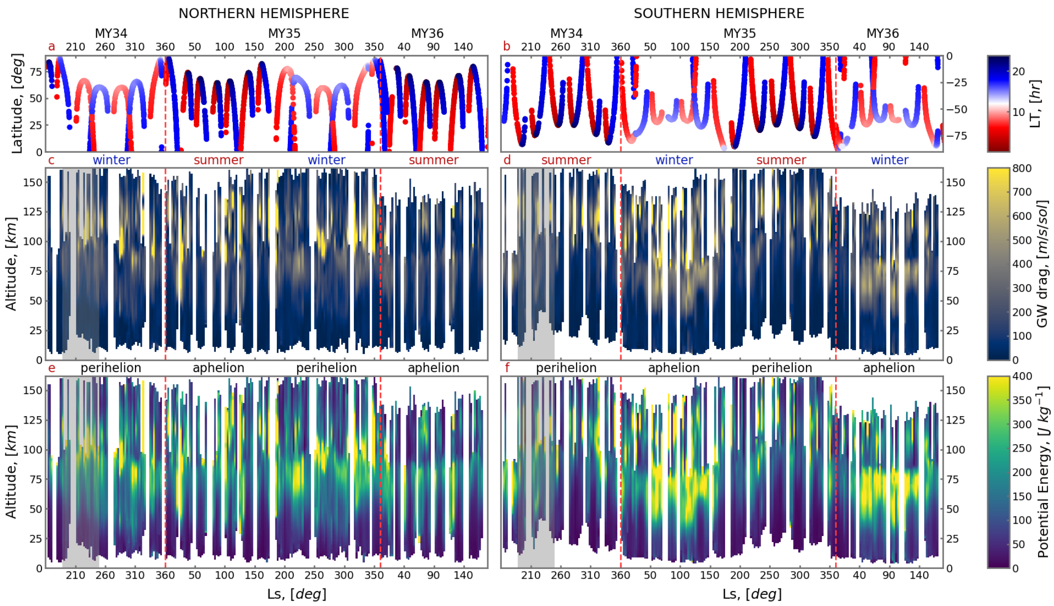

Figure 3. Upper row: coverage of the ACS measurements as a function of the solar longitude L_s and latitude; color indicates the local time of observations. Middle and lower rows: seasonal-altitude distribution for the GW drag and potential energy (per unit mass), correspondingly. The left and right columns present the data for the Northern and Southern hemispheres, respectively. Grey area denotes the period of global dust storm (GDS). Red dashed lines separate Martian years MY34, MY35 and MY36.

mospheric altitudes. In the summer hemispheres, the peaks of wave activity lie higher, with GW drag reaching maxima near or above the mesopause.

5 Latitudinal Distribution

We next turn to a more detailed examination and consider the altitude-latitude distributions of the GW characteristics. For that, we gathered data into 3° latitude bins and organized the results into four seasons centered around $L_s = 0$, 90°, 180° and 270°. They represent two equinoctial seasons ($L_s = 0°$ and 180°) and two solstitial ones: around the aphelion ($L_s = 90°$) and perihelion ($L_s = 270°$). In order to eliminate the influence of the major dust storm of MY34 that occurred between $Ls = 188°$ and 250°, we excluded those measurements. The differences in the GW activity introduced by the GDS are explicitly considered in the next section. The cross-sections of the GW potential energy are plotted in Figure 4. It is immediately seen that the wave activity is stronger in the first half of the Martian year. The maxima are located in low latitudes in the upper mesosphere and lower thermosphere during the equinoctial $L_s = 0°$ season (panel a) and shifted to the southern (winter) hemisphere over the solstitial $L_s = 90°$ season (panel b). A similar pattern occurs in the second half of the year, although with a clearly smaller magnitude, especially during the northern winter solstice. Note the symmetry of the E_p distribution with respect to the equator during the equinox.

Figure 5 provides further insight into the climatology of GWs. It presents the latitude-altitude distributions of the zonal GW drag (shaded) along with the mean zonal wind (red contours) simulated with the MAOAM Martian general circulation model (MGCM) (Hartogh et al., 2005; Medvedev & Hartogh, 2007) for MY34 and 35 and accordingly av-

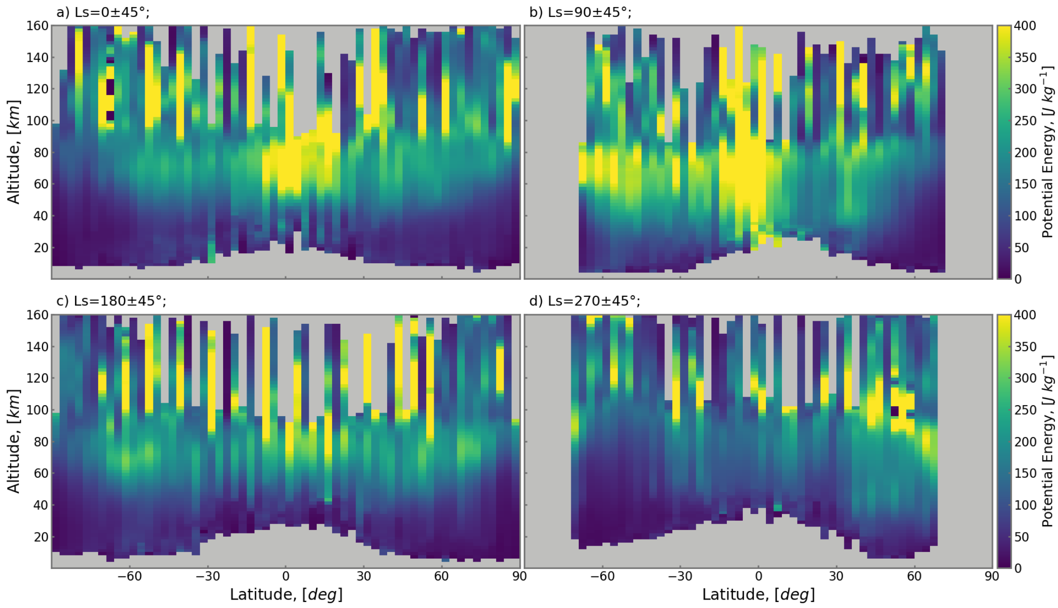

Figure 4. Latitude-altitude distributions of the retrieved wave potential energy (per unit mass) E_p for four representative seasons centered around a) $L_s = 0°$, b) $90°$, c) $180°$ and d) $270°$. The period of the MY34 GDS is excluded.

eraged. It is seen that the regions of large GW drag in general align with the areas of relatively weak zonal wind, which agrees with the theoretically expected propagation and dissipation characteristics of gravity waves. Harmonics, especially the ones with relatively slow (ground-based) horizontal phase speeds c, are substantially damped, when their phase speeds approach the mean wind $\bar{u}$. This decrease in the intrinsic horizontal phase speed $|c - \bar{u}|$ causes absorption of a significant portion of GWs propagating along the mean wind $\bar{u}$. Harmonics having $c > \bar{u}$ or traveling in the opposite to the wind direction can avoid wave filtering and propagate higher, grow in amplitude and ultimately break down when wave-induced wind fluctuations $|u'|$ approach the intrinsic phase speed $|c-\bar{u}|$. The smaller $\bar{u}$, the smaller amplitude $|u'|$ is required for breaking/saturation, which is illustrated by the enhanced momentum deposition in the regions of the weak mean wind shown in Figure 5.

The equinoctial circulation consists of two prograde (eastward) jets centered in middle-to-high latitudes of each hemisphere and the region of weak winds at low latitudes. The inferred distribution of the GW drag reflects this pattern of inter-hemispheric symmetry. Weaker mean winds in low latitudes allow for GW breaking at lower altitudes. The mean wind changes direction to retrograde (westward) above the mesopause. This causes harmonics traveling westward ($c < 0$) to break and/or dissipate and deposit their momentum there. In fact, the wind reversal itself is the result of the GW drag (Medvedev et al., 2011a, 2011b, 2013).

The solstitial circulation features eastward/westward jets in the winter/summer hemispheres. The jets are stronger during the perihelion solstices, as seen from the comparison of Figures 5b and d, due to greater insolation and larger meridional temperature and pressure gradients in this season. Assuming that GW harmonics excited in the lower atmosphere have a broad range of phase speeds c and travel in all horizontal directions, stronger background winds $\bar{u}$ filter out more waves propagating in the same direction. The remaining harmonics must acquire larger amplitudes in order to break down and,

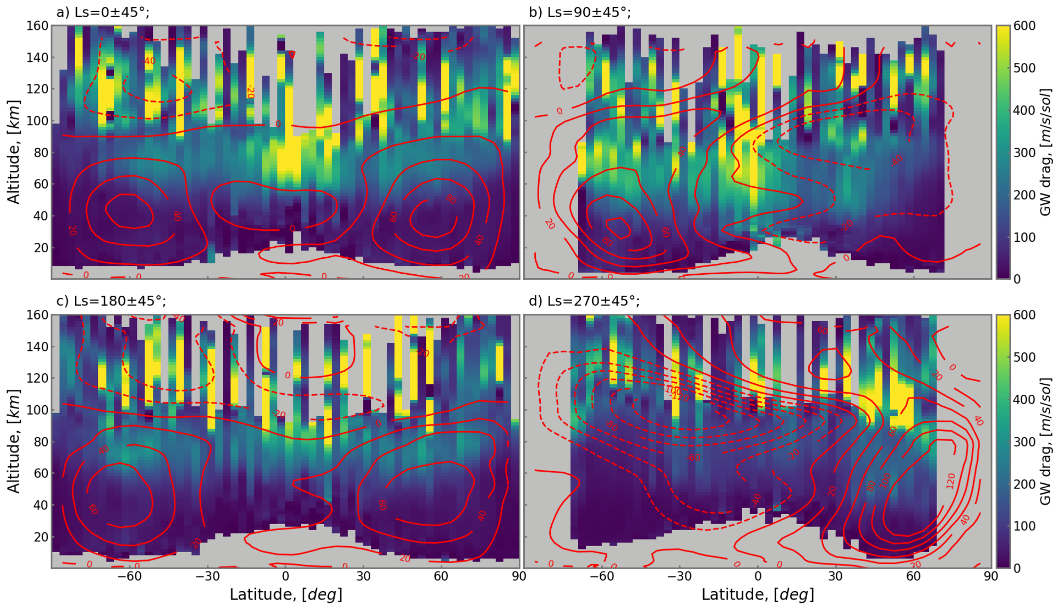

Figure 5. The same as in Figure 4, but for the momentum forcing (or GW drag) in m s^{-1} sol^{-1} (shaded). The simulations with the MAOAM MGCM of the mean zonal wind corresponding to the same intervals of L_s is shown with contour lines. Solid and dashed lines represent eastward and westward winds, respectively. The data for the period of the MY34 GDS are excluded.

therefore, have to propagate higher. This mechanism explains why the GW drag is localized in a relatively narrow altitude range during the perihelion solstice (Figure 5d) compared to that during the aphelion (Figure 5b).

6 Impact of the Dust Storm

As was mentioned above, a global dust storm (GDS) rapidly developed in MY34 around $L_s = 188°$ and decayed by $L_s = 250°$. The dust load over the same period of MY35 was close to normal with a minor enhancement between $L_s = 230°$ and $250°$. Figure 6 presents the latitude-altitude distributions of the retrieved GW potential energy and drag averaged over the corresponding periods along with their differences (right column). The latter show several systematic features introduced by the storm. First, the changes are mostly symmetric with respect to the equator, at least in the overlapping bins. They may reflect the predominantly symmetric global equinoctial circulation at the beginning of the storm, which affects generation and vertical propagation of GW harmonics. Second, a distinct reduction of wave activity occurs in middle latitudes between $\sim$15° and 70° in both hemispheres. A similar behavior during the MY34 GDS was observed in the Mars Climate Sounder data by Heavens et al. (2020) throughout the lower atmosphere below $\sim$30 km. Simulations with a high-resolution global circulation model also reproduced the approximately factor 2 decrease of the GW potential energy in the lower and middle atmosphere (Kuroda et al., 2020). It was related to the reduction of wave generation caused by convective and baroclinic stabilization of the atmosphere induced by the storm. The same simulations predicted a gradual increase of GW activity with height, such that E_p exceeds the "low dust" values near the top of the model domain at around 80 km. Further observational evidence for the enhancement of GW activity in the upper atmosphere during dust storms was provided in the work by Yiğit,

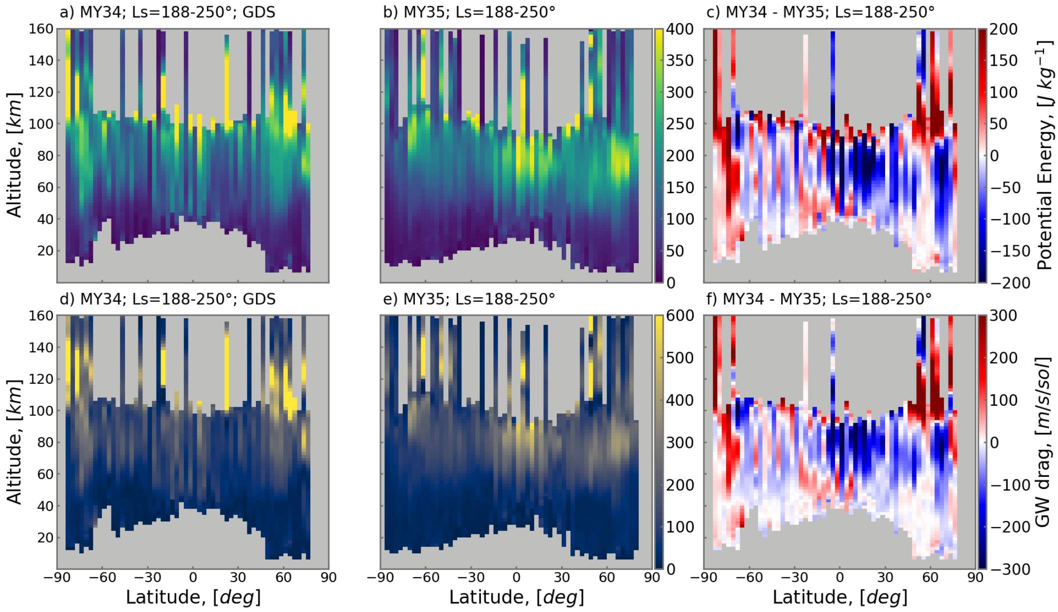

Figure 6. Altitude-latitude cross-sections of wave potential energy (upper row) and drag (lower row) retrieved during the global dust storm of MY34 (L_s=188°–250°, left column) and the corresponding low-dust period of MY35 (middle column). The differences between the observations of MY34 and MY35 are shown in the right column.

Medvedev, Benna, and Jakosky (2021) based on NGIMS measurements on board the MAVEN orbiter. Those measurements covered the thermosphere between 160 and 230 km, that is above the upper limit of the MIR data presented here. A several latitudinal bins in Figures 6a,d with data extending above ∼100 km and available for comparison point out to a dust-induced enhancement of GW activity and drag above the mesopause.

The results in Figure 6 show two additional features, which were neither observed, nor modeled/predicted before. One of them is the enhancement of the GW activity at all heights in the polar regions, which is clearly seen in the southern hemisphere and is somewhat less apparent in the northern one. The second is the strong increase of GW activity and drag below 60 km during the GDS and a steep reduction above in low latitudes (approximately within ±15° from the equator). While the polar enhancement is a sufficiently robust feature, the equatorial pattern can be an artifact of a much sparser coverage (see Figure 3, upper panels). Timing of observations can also be a source of biases due to variations of the GW field with local time. They are discussed in the next section.

7 Local Time Variations

7.1 Changes due to the Dust Storm

The relatively small number of observations in low to middle latitudes provides no opportunity to further evaluate the dust storm-induced pattern in the equatorial zone shown in Figure 6, or the local time behavior there. However, the high-latitude enhancement can be considered in more detail. For that, we plotted in Figure 7 the local time variations of the GW potential energy averaged over latitudes higher than 60° in both hemispheres. It is seen that, in both Martian years, most of the observations in the southern high latitudes were taken during nighttime, and during daytime in the northern hemi-

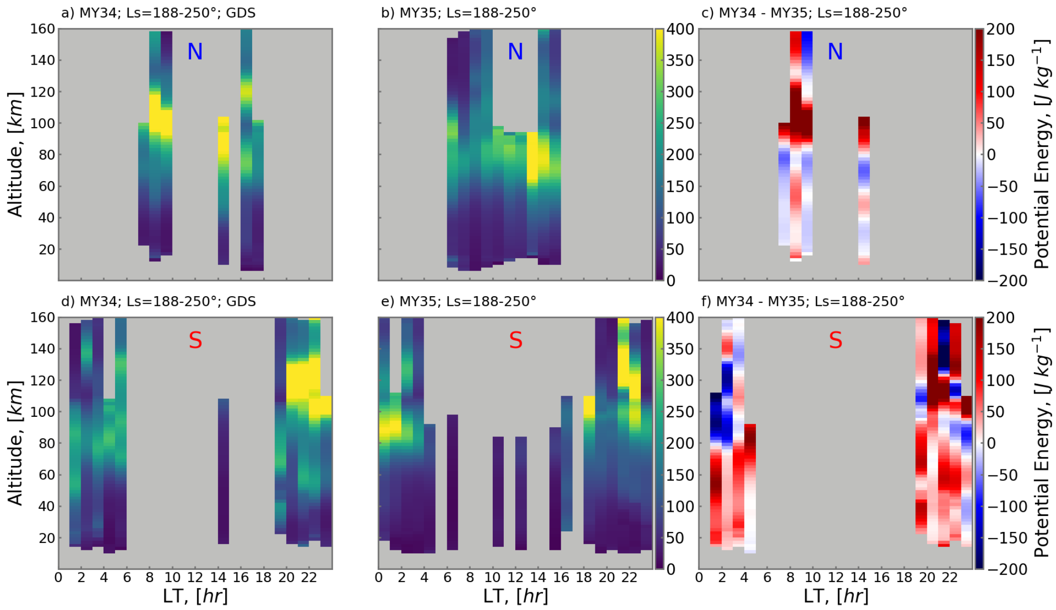

Figure 7. Local time variations of the globally averaged wave potential energy observed during the GDS of MY34 (L_s=188°–250°, left column) and the corresponding "low dust" period of MY35 (middle column). The differences between the observations of MY34 and MY35 are shown in the right column. The observations in high northern (Lat > 60°N) and high southern (Lat > 60°S) latitudes are shown in the upper and lower rows, respectively.

sphere. Given that the location (latitudes) and timing (seasons and local times) of the observations are the same in MY34 and 35, the differences in the GW activity can be attributed to the dust conditions. A clear enhancement of E_p during the dust storm occurs in the southern high latitudes of the middle and upper atmosphere. There are fewer overlapping observations in the northern hemisphere, but those available demonstrate the increased GW activity in the thermosphere as well. Note that high-latitude dust storm-induced enhancements in the middle atmosphere of the similar magnitude were predicted in simulations with a wave-resolving MGCM up to ∼80 km (Kuroda et al., 2020, Figure 4b). The results presented here provide the first observational validation for this modeling prediction and, also demonstrate that the enhancement extends higher into the thermosphere up to ∼160 km.

7.2 Seasonal Behavior

After exploring the impact of the major dust storm on local time variations of the GW field, we next consider how they evolve seasonally. For that, we grouped the data into the same four seasons discussed in Section 5 and plotted them as functions of local time in Figure 8. The figure reveals more intraday features of the GW activity. They include, in particular, a downward phase progression, which is more clearly seen during equinoctial seasons (Figures 8a,c). Such local time variations can reflect a modulation of GWs in the middle and upper atmosphere by the diurnal and semi-diurnal thermal tides, which have a distinct latitudinal structure and vary with seasons (Yiğit & Medvedev, 2017; Kumar et al., 2022). Tides are more symmetric with respect to the equator during equinoxes due to the position of the Sun. Therefore, averaging over all latitudes does not mask the tidal signal in Figures 8a,c that much as it does during the solstitial seasons. A mixture of modulation by the semidiurnal and diurnal tides is seen during the

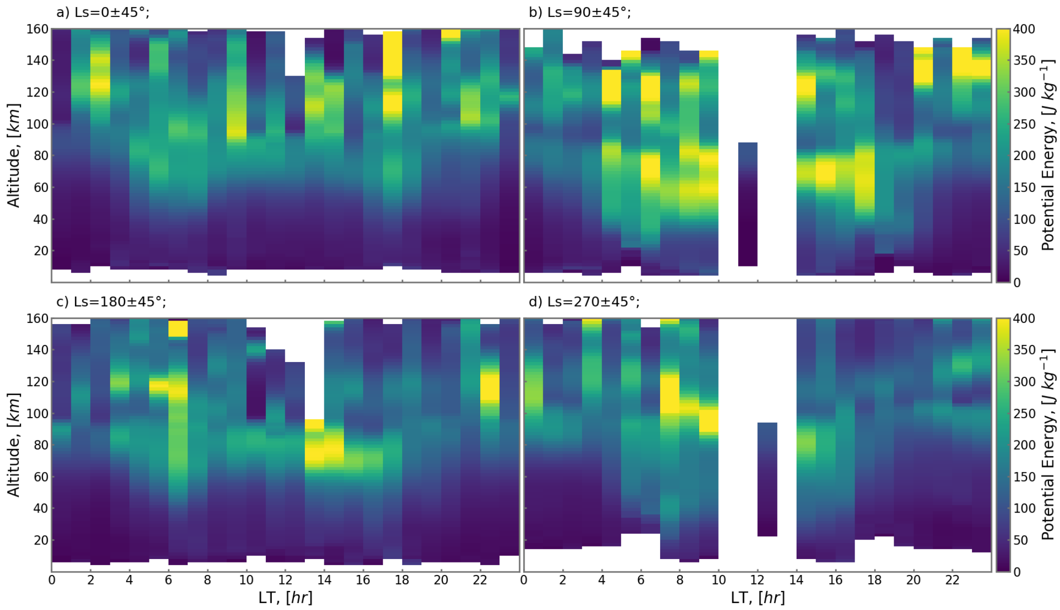

Figure 8. Local time variations of the GW potential energy at four representative seasons centered around $Ls = 0°$, $90°$, $180°$ and $270°$. The data for the MY34 GDS are excluded.

$L_s = 0°$ equinox, while the diurnal (24-hour period) variation dominates the $L_s = 180°$ season. Figures 8b,d show stronger GW activity in the first half of the day with signs of the downward phase progression. The latitudinal distribution of tides is more complex due to the shifted center of solar heating and differences in the background winds. Thus, the peculiarities in the intraday variations of E_p in Figures 8b,d may reflect this and the biases due to the measurements sampling. Note that variations can be caused by intraday changes in GW sources, which, however, were not detected in the considered data set. Besides, the behavior of the phase provides unambiguous evidence for the tidal nature of the GW activity variations.

8 Conclusions

We presented the results of the analysis of gravity waves (GWs) retrieved from solar occultation measurements by NIR and MIR channels of the ACS instrument on board the Trace Gas Orbiter (TGO) taken over two Martian years (mid-MY34 to mid-MY36). The retrieved temperature profiles spanning altitudes up to 100 km (NIR) and 160 km (MIR) were separated into mean component and disturbances, which were used for characterizing the wave field. In particular, the wave activity represented by wave potential energy E_p and the dynamical impact on the mean flow in terms of the GW momentum deposition (“drag”) are considered here. The main inferences of this study are as follows:

1. GWs are present at all times and places in the Martian atmosphere. Within the considered dataset, we did not find any time period or location (except for a few profiles of questionable quality) when and where GW disturbances were absent.
2. Wave activity is distributed symmetrically with respect to the equator during the equinoctial seasons, while the maximum is shifted to the winter hemisphere during solstices.

3. Maxima of GW drag align with the areas of weak zonal wind along the edges of seasonally varying zonal jets. This feature agrees well with physics of GW-mean flow interactions.
4. During the MY34 GDS, observed GWs were depleted in middle latitudes of both hemispheres. In contrast, GW activity increased at high latitudes (poleward of $\sim 60°$).
5. During both equinoctial seasons we observed diurnal and semidiurnal modulation of the GW activity and drag with the downward phase progression.

The climatology of the GW activity and drag in the middle and upper atmosphere based on 2 Martian years of ACS observations confirms theoretical/modeling predictions, on one hand. On the other hand, it reveals new features (like enhancements of wave activity in low latitudes), which were not anticipated and, given the dynamical importance of GWs, have to be accounted for in numerical models. ACS continues observations, and new data will help to further elucidate the spatio-temporal behavior of the GW field.

9 Data Availability Statement

The ACS data are available from ESA Planetary Science Archive (PSA) (`https://archives.esac.esa.int/psa/%23!Table%20View/ACS=instrument#!Home%20View`). The temperature vertical profiles retrieved from ACS-NIR and ACS-MIR measurements are described in (Fedorova et al., 2023; Belyaev et al., 2022) and available at (Fedorova, 2022; Belyaev, 2022), respectively. The most recent MAOAM model output can be accessed at `https://mars.mipt.ru`. The vertical profiles of background temperature, wave temperature disturbance, amplitude and GW drag are available at `https://data.mendeley.com/datasets/7d9b2kjfby/1` (Starichenko, 2023).

Acknowledgments

The ExoMars is a joint mission of the European Space Agency (ESA) and Roscosmos. The ACS experiment is led by the Space Research Institute (IKI) in Moscow, assisted by LATMOS in France. The science operations of ACS are funded by Roscosmos and ESA. The authors affiliated with IKI acknowledge funding from the Ministry of Science and Higher Education of the Russian Federation (subsidies, theme "Planeta"). The authors affiliated with LATMOS acknowledge funding from the Centre National d'Etudes Spatiales (CNES) and the Centre National de la Recherche Scientifique (CNRS).

References

Ando, H., Imamura, T., & Tsuda, T. (2012). Vertical wavenumber spectra of gravity waves in the Martian atmosphere obtained from Mars Global Surveyor radio occultation data. *Journal of the Atmospheric Sciences*, *69*, 2906–2912. doi: 10.1175/JAS-D-11-0339.1

Belyaev, D. (2022). *Thermal Structure of the Middle and upper Atmosphere of Mars from ACS/TGO CO2 spectroscopy. Mendeley Data. V2.* doi: https://doi.org/10.17632/g6j5t2z73z.2

Belyaev, D., Fedorova, A., Trokhimovskiy, A., Alday, J., Montmessin, F., Korablev, O., & et al. (2021). Revealing a high water abundance in the upper mesosphere of Mars with ACS onboard TGO. *Geophysical Research Letters*, *48*(e2021GL093411). doi: 10.1029/2021GL093411

Belyaev, D., Fedorova, A., Trokhimovskiy, A., Alday, J., Montmessin, F., & Korablev, O. e. a. (2022). Thermal Structure of the Middle and Upper Atmosphere of Mars from ACS/TGO CO2 Spectroscopy. *Journal of Geophysical Research: Planets*, *127*(10), e2022JE007286. doi: https://doi.org/10.1029/2022JE007286

Brown, Z., Medvedev, A., Starichenko, E., Koskinen, T., & Müller-Wodarg, I. (2022). Evidence for Gravity Waves in the Thermosphere of Saturn and Implications for Global Circulation. *Geophysical Research Letters*, *49*(e2021GL097219). doi: 10.1029/2021GL097219

Creasey, J. E., Forbes, J. M., & Hinson, D. P. (2006b). Global and seasonal distribution of gravity wave activity in Mars' lower atmosphere derived from MGS radio occultation data. *Geophysical Research Letters*, *33*. doi: 10.1029/2005GL024037

Creasey, J. E., Forbes, J. M., & Keating, G. M. (2006a). Density variability at scales typical of gravity waves observed in Mars' thermosphere by the MGS accelerometer. *Geophysical Research Letters*, *33*(L22814). doi: 10.1029/2006GL027583

England, S. L., Liu., G., Yiğit, E., Mahaffy, P. R., Elrod, M., Benna, M., … Jakosky, B. (2017). MAVEN NGIMS observations of atmospheric gravity waves in the Martian thermosphere. *Journal of Geophysical Research: Space Physics*, 2310–2335. doi: 10.1002/2016JA023475

Ern, M., Preusse, P., Alexander, M. J., & Warner, C. D. (2004). Absolute values of gravity wave momentum flux derived from satellite data. *Journal of Geophysical Research: Atmospheres*, *109*. doi: 10.1029/2004JD004752

Fedorova, A. (2022). *Water vapor saturation state on Mars from ACS-NIR/TGO occultations from MY34 to MY36. Mendeley Data, V1.* doi: https://doi.org/10.17632/6xrn9v4dc5.1

Fedorova, A., Montmessin, F., Korablev, O., Luginin, M., Trokhimovskiy, A., Belyaev, D., & et al. (2020). Stormy water on Mars: The distribution and saturation of atmospheric water during the dusty season. *Science*, *367*, 297–300. doi: 10.1126/science.aay9522

Fedorova, A., Montmessin, F., Trokhimovskiy, A., Luginin, M., Korablev, O., Alday, J., … Shakun, A. (2023). A two-Martian years survey of the water vapor saturation state on Mars based on ACS NIR/TGO occultations. *Journal of Geophysical Research: Planets*, *128*(1), e2022JE007348. doi: 10.1029/2022JE007348

Fritts, D. C., & Alexander, J. M. (2003). Gravity wave dynamics and effects in the middle atmosphere. *Reviews of Geophysics*, *41*(1), 1003. doi: 10.1029/2001RG000106

Fritts, D. C., Wang, L., & Tolson, R. H. (2006). Mean and gravity wave structures and variability in the Mars upper atmosphere inferred from Mars Global Surveyor and Mars Odyssey aerobraking densities. *Journal of Geophysical Research*, *111*(A12304). doi: 10.1029/2006JA011897

Gilli, G., Forget, F., Spiga, A., Navarro, T., Millour, E., Montabone, L., & et al. (2020). Impact of gravity waves on the middle atmosphere of Mars: A non-orographic gravity wave parameterization based on global climate modeling and MCS observations. *Journal of Geophysical Research: Planets*, *125*(e2018JE005873). doi: 10.1029/2018JE005873

Hartogh, P., Medvedev, A. S., Kuroda, T., Saito, R., Villanueva, G., Feofilov, A. G., … Berger, U. (2005). Description and climatology of a new general circulation model of the Martian atmosphere. *Journal of Geophysical Research*, *110*. doi: 10.1029/2005JE002498

Heavens, N. G., Kass, D. M., Kleinböhl, A., & Schofield, J. T. (2020). A multiannual record of gravity wave activity in Mars's lower atmosphere from on-planet observations by the Mars Climate Sounder. *Icarus*, *341*, 113630. doi: 10.1016/j.icarus.2020.113630

Hinson, D. P., Simpson, R. A., Twicken, J. D., Tyler, G. L., & Flasar, F. M. (1999). Initial results from radio occultation measurements with Mars Global Surveyor. *Journal of Geophysical Research: Planets*, *104*(E11), 26997–27012. doi: 10.1029/1999JE001069

Hinson, D. P., & Tyler, G. (1983). Internal gravity waves in Titan's atmosphere observed by Voyager radio occultation. *Icarus*, *54*(2), 337-352. doi: https://doi.org/10.1016/0019-1035(83)90202-6

Keating, G. M., Bougher, S. W., Zurek, R. W., Tolson, R. H., Cancro, G. J., Noll, S. N., ... Babicke, J. M. (1998). The Structure of the Upper Atmosphere of Mars: In Situ Accelerometer Measurements from Mars Global Surveyor. *Science*, *279*(5357), 1672–1676. doi: 10.1126/science.279.5357.1672

Korablev, O., Montmessin, F., Trokhimovskiy, A., Fedorova, A., Shakun, A., Grigoriev, A., & et al. (2018). The Atmospheric Chemistry Suite (ACS) of three spectrometers for the ExoMars 2016 Trace Gas Orbiter. *Space Science Reviews*, *214*(7). doi: 10.1007/s11214-017-0437-6

Kumar, A., England, S. L., Liu, G., Jain, S., & Schneider, N. M. (2022). Observations of atmospheric tides in the middle and upper atmosphere of Mars from MAVEN and MRO. *Journal of Geophysical Research: Planets*, *127*(8), e2022JE007290. doi: https://doi.org/10.1029/2022JE007290

Kuroda, T., Medvedev, A. S., & Yiğit, E. (2020). Gravity wave activity in the atmosphere of Mars during the 2018 global dust storm: Simulations with a high-resolution model. *Journal of Geophysical Research: Planets*, *125*(11). doi: 10.1029/2020JE006556

Kuroda, T., Medvedev, A. S., Yiğit, E., & Hartogh, P. (2015). A global view of gravity waves in the Martian atmosphere inferred from a high-resolution general circulation model. *Geophysical Research Letters*, *42*, 9213-9222. doi: 10.1002/2015GL066332

Kuroda, T., Medvedev, A. S., Yiğit, E., & Hartogh, P. (2016). Global distribution of gravity wave sources and fields in the Martian atmosphere during equinox and solstice inferred From a high-resolution general circulation model. *Journal of the Atmospheric Sciences*, *73*. doi: 10.1175/JAS-D-16-0142.1

Kuroda, T., Yiğit, E., & Medvedev, A. S. (2019). Annual cycle of gravity wave activity derived from a high-resolution Martian general circulation model. *Journal of Geophysical Research: Planets*, *124*(6), 1618–1632. doi: 10.1029/2018JE005847

Leelavathi, V., Venkateswara Rao, N., & Rao, S. V. B. (2020). Interannual variability of atmospheric gravity waves in the Martian thermosphere: Effects of the 2018 planet-encircling dust event. *Journal of Geophysical Research: Planets*, *125*(12), e2020JE006649. doi: 10.1029/2020JE006649

Medvedev, A. S., & Hartogh, P. (2007). Winter polar warmings and the meridional transport on Mars simulated with a general circulation model. *Icarus*, *186*, 97–110.

Medvedev, A. S., & Yiğit, E. (2019). Gravity waves in planetary atmospheres: Their effects and parameterization in global circulation models. *Atmosphere*, *10*(9). doi: 10.3390/atmos10090531

Medvedev, A. S., Yiğit, E., & Hartogh, P. (2011a). Estimates of gravity wave drag on mars: Indication of a possible lower thermospheric wind reversal. *Icarus*, *211*, 909-912. doi: 10.1016/j.icarus.2010.10.013

Medvedev, A. S., Yiğit, E., Hartogh, P., & Becker, E. (2011b). Influence of gravity waves on the Martian atmosphere: General circulation modeling. *Journal of Geophysical Research*, *116*(E10004). doi: 10.1029/2011JE003848

Medvedev, A. S., Yiğit, E., Kuroda, T., & Hartogh, P. (2013). General circulation modeling of the Martian upper atmosphere during global dust storms. *Journal of Geophysical Research: Planets*(10), 2234–2246. doi: 10.1002/2013JE004429

Nakagawa, H., Terada, N., Jain, S. K., Schneider, N. M., Montmessin, F., Yelle, R. V., ... Jakosky, B. M. (2020). Vertical propagation of wave perturbations in the middle atmosphere on Mars by MAVEN/IUVS. *Journal of Geophysical Research: Planets*, *125*(9), e2020JE006481. doi: https://doi.org/10.1029/2020JE006481

Rao, N. V., Leelavathi, V., & Rao, S. V. B. (2021). Variability of temperatures and gravity wave activity in the Martian thermosphere during low solar irradiance. *Icarus*(114753). doi: 10.1016/j.icarus.2021.114753

Roeten, K. J., Bougher, S. W., Yiğit, E., Medvedev, A. S., Benna, M., & Elrod, M. K. (2022). Impacts of gravity waves in the Martian thermosphere: The Mars Global Ionosphere-Thermosphere model coupled with a whole atmosphere gravity wave scheme. *Journal of Geophysical Research: Planets*, *127*, e2022JE007477. doi: https://doi.org/10.1029/2022JE007477

Seiff, A., & Kirk, D. B. (1976). Structure of Mars' Atmosphere up to 100 Kilometers from the Entry Measurements of Viking 2. *Science*, *194*(4271), 1300-1303. doi: 10.1126/science.194.4271.1300

Starichenko, E. D. (2023). *Climatology of Gravity Wave Activity From Two Martian Years of ACS/TGO Observations*. Mendeley Data, V1. doi: 10.17632/7d9b2kjfby.1

Starichenko, E. D., Belyaev, D. A., Medvedev, A. S., Fedorova, A. A., Korablev, O. I., Trokhimovskiy, A., ... Hartogh, P. (2021). Gravity wave activity in the Martian atmosphere at altitudes 20–160 km from ACS/TGO occultation measurements. *Journal of Geophysical Research: Planets*, *126*(8), e2021JE006899. doi: https://doi.org/10.1029/2021JE006899

Terada, N., Leblanc, F., Nakagawa, H., Medvedev, A. S., Yiğit, E., Kuroda, T., ... Jakosky, B. M. (2017). Global distribution and parameter dependences of gravity wave activity in the Martian upper thermosphere derived from MAVEN/NGIMS observations. *Journal of Geophysical Research: Space Physics*, *122*(2), 2374–2397. doi: 10.1002/2016JA023476

Vals, M., Spiga, A., Forget, F., Millour, E., Montabone, L., & Lott, F. (2019). Study of gravity waves distribution and propagation in the thermosphere of Mars based on MGS, ODY, MRO and MAVEN density measurements. *Planetary and Space Science*, *178*(104708). doi: 10.1016/j.pss.2019.104708

Wright, C. J. (2012). A one-year seasonal analysis of Martian gravity waves using MCS data. *Icarus*, *219*(1), 274–282. doi: 10.1016/j.icarus.2012.03.004

Yiğit, E., England, S. L., Liu, G., Medvedev, A. S., Mahaffy, P. R., Kuroda, T., & Jakosky, B. M. (2015). High-altitude gravity waves in the Martian thermosphere observed by MAVEN/NGIMS and modeled by a gravity wave scheme. *Geophysical Research Letters*, *42*(21), 8993–9000. doi: 10.1002/2015GL065307

Yiğit, E., & Medvedev, A. S. (2015). Internal wave coupling processes in Earth's atmosphere. *Advances in Space Research*, *55*(4), 983–1003. doi: 10.1016/j.asr.2014.11.020

Yiğit, E., & Medvedev, A. S. (2017). Influence of parameterized small-scale gravity waves on the migrating diurnal tide in Earth's thermosphere. *Journal of Geophysical Research: Space Physics*, *122*, 4846–4864. doi: 10.1002/2017JA024089

Yiğit, E., Medvedev, A. S., Benna, M., & Jakosky, B. M. (2021). Dust storm-enhanced gravity wave activity in the Martian thermosphere observed by MAVEN and implication for atmospheric escape. *Geophysical Research Letters*. doi: 10.1029/2020GL092095

Yiğit, E., Medvedev, A. S., & Hartogh, P. (2018). Influence of gravity waves on the climatology of high-altitude Martian carbon dioxide ice clouds. *Annales Geophysicae*, *36*(6), 1631–1646. doi: 10.5194/angeo-36-1631-2018

Yiğit, E., Medvedev, A. S., & Hartogh, P. (2021). Variations of the Martian Thermospheric Gravity-wave Activity during the Recent Solar Minimum as Observed by MAVEN. *The Astrophysical Journal*, *920*(69). doi: 10.3847/1538-4357/ac15fc

Yiğit, E. (2023). Coupling and interactions across the Martian whole atmosphere system. *Nature Geoscience*, 1–10. doi: 10.1038/s41561-022-01118-7

Yiğit, E., Aylward, A. D., & Medvedev, A. S. (2008). Parameterization of the effects of vertically propagating gravity waves for thermosphere general circulation models: Sensitivity study. *Journal of Geophysical Research*, *113*(D19), D19106. doi: 10.1029/2008JD010135

Young, L. A., Yelle, R. V., Young, R., Seiff, A., & Kirk, D. B. (1997). Gravity waves in Jupiter's thermosphere. *Science*, *276*(5309), 108-111. doi: 10.1126/science.276.5309.108

Young, R. E., Walterscheid, R. L., Schubert, G., Seiff, A., Linkin, V. M., & Lipatov, A. N. (1987). Characteristics of gravity waves generated by surface topography on Venus: Comparison with the VEGA balloon results. *Journal of Atmospheric Sciences*, *44*(18), 2628 - 2639. doi: 10.1175/1520-0469(1987)044⟨2628:COGWGB⟩2.0.CO;2